Analysis of the Future Potential of Autoencoders in Industrial Defect Detection

Sarah Schneider[1,2], Doris Antensteiner[1], Daniel Soukup[1] and Matthias Scheutz[2]
[1]*High-Performance Vision Systems, Center for Vision, Automation and Control, AIT Austrian Institute of Technology, Vienna, Austria*
[2]*Human-Robot Interaction Lab, Tufts University, Medford, MA, U.S.A.*

Keywords: Autoencoder, Anomaly Detection, Computer Vision, One-class Learning.

Abstract: We investigated the anomaly detection behaviour of three convolutional autoencoder types - a "standard" convolutional autoencoder (CAE), a variational convolutional autoencoder (VAE) and an adversarial convolutional autoencoder (AAE) - by applying them to different visual anomaly detection scenarios. First, we utilized our three autoencoder types to detect anomalous regions in two synthetically generated datasets. To investigate the convolutional autoencoders' defect detection performances "in the industrial wild", we applied the models on quality inspection images of non-defective and defective material regions. We compared the performances of all three autoencoder types based on their ability to detect anomalies and captured the training complexity by measuring the time needed for training them. Although the CAE is the simplest model, the trained model performed nearly as well as the more sophisticated autoencoder types, which depend on more complex training processes. For data that lacks regularity or shows purely stochastic patterns, all our autoencoders failed to compute meaningful results.

1 INTRODUCTION

The detection of defective material is an essential component in the industrial manufacturing process. Yang et al. (2020) describe how the detection of defective material represents a complex problem due to the elusive nature and immense diversity of the defects. Pang et al. (2021) elaborate in much detail how anomalies deviate from what is defined as usual or regarded as normal and explain the process of anomaly detection - the detection of data instances that differ from the majority of samples.

An autoencoder (Rumelhart and McClelland, 1987) consists of an encoder and a decoder model. The encoder network encodes data into a compressed version, the decoder network decodes it back such that it is as similar as possible to the original input. Due to this underlying principle of learning and compressing normal data into a latent vector by minimizing the reconstruction error, the autoencoder is an appropriate tool for anomaly detection. By training an autoencoder model purely on normal data, it will learn the profile of non-anomalous data and the resulting reconstruction error for normal data will be lower than the reconstruction error for anomalous data.

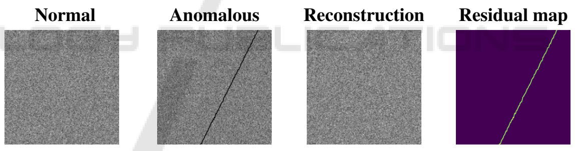

Figure 1: Principle of autoencoder based anomaly detection: The autoencoder is trained exclusively on normal images. If that trained model is applied on an anomalous image, the input is reconstructed by using the mapping the model learned from the non-anomalous data. The reconstruction then deviates from the anomalous image at pixel positions where the anomalies appear, see the residual map.

By considering non-defective material as normal and defective material as anomalous, the detection of defects on material surfaces can be formulated as an anomaly detection problem. Autoencoders have been previously used to detect defects, e. g., Essid et al. (2018) demonstrated how autoencoders can be utilized to localize defects on metal boxes and Kholief et al. (2017) used autoencoders for the detection of surface defects on steel strips.

We compared three convolutional versions of autoencoders - a "standard" autoenocoder (CAE) (Gondara, 2016), a variational autoencoder (VAE) (Kingma and Welling, 2014) and an adversarial au-

DOI: 10.5220/0010777000003124
In *Proceedings of the 17th International Joint Conference on Computer Vision, Imaging and Computer Graphics Theory and Applications (VISIGRAPP 2022) - Volume 4: VISAPP*, pages 282-289
ISBN: 978-989-758-555-5; ISSN: 2184-4321

toencoder (AAE) (Makhzani et al., 2016).
First, we used two datasets we generated synthetically. Both consist of a ground structure considered as normal or non-defective. In the corresponding anomalous images, the ground structure was changed in order to create anomalous regions. The pixel-wise reconstruction error can be used to localize anomalous regions. We can quantify the quality of our anomaly detection algorithm because the location of anomalous pixels are exactly known.

To investigate the anomaly detection behaviour of autoencoders in the "industrial wild", our models are utilized to detect defects in quality inspection images of two different manufactured materials, namely *material 1* and *material 2*.

Our investigations show scenarios in which a convolutional autoencoder leads to meaningful results, but we also present a situation where a convolutional autoencoder fails to detect anomalies. To capture the "cost-benefit ratio" of our different autoencoder types, we evaluated the quality of their anomaly detection results alongside with their measured training times.

Our contribution comprises:

- a thorough review and suggestions for improved designs based on the given evidence,
- a quantitative and qualitative comparison of different convolutional autoencoder types (CAE, VAE, AAE) based on their anomaly localization performances on two synthetic datasets,
- a qualitative evaluation of the performances of different convolutional autoencoder types (CAE, VAE, AAE) on two industrial datasets.

2 AUTOENCODERS FOR ANOMALY DETECTION

The underlying principle of autoencoders is to encode an input sample $\mathbf{x} \in \mathbb{R}^{C\times H\times W}$ into a compressed representation $\mathbf{z} \in \mathbb{R}^{C_b\times H_b\times W_b}$ and then decoding this representation back such that it is as similar to the original input as possible. Typically, the dimensions of the so-called bottleneck layer $C_b \times H_b \times W_B$ are significantly smaller than the input dimensions $C \times H \times W$. This enforces a compression of data. By training the autoencoder purely on normal samples, it will learn the profile of these normal images. A normal image region will be reconstructed more accurately than an anomalous region. The residual map $\mathbf{R}(\mathbf{x},\tilde{\mathbf{x}}) \in \mathbb{R}^{C\times H\times W}$ formulates the squared pixel-wise difference of the input $\mathbf{x}$ and its reconstruction $\tilde{\mathbf{x}}$ computed by the trained network and can be utilized to decide between normal and anomalous pixels (Bergmann et al., 2019; Bank et al., 2020; Manakov et al., 2019).

$$\mathbf{R}(\mathbf{x},\tilde{\mathbf{x}}) = (\mathbf{x}-\tilde{\mathbf{x}})^2 \tag{1}$$

2.1 "Standard" Convolutional Autoencoder

A "standard" convolutional autoencoder as described in Bergmann et al. (2019) and Manakov et al. (2019) consists of a convolutional encoder network E_{CAE}, which compresses the data $\mathbf{x}$ into a latent representation $\mathbf{z}$ and another convolutional network, the decoder D_{CAE}, which outputs a reconstruction $\tilde{\mathbf{x}}$ of the compressed version of the data:

$$\tilde{\mathbf{x}} = D_{CAE}(E_{CAE}(\mathbf{x})) = D_{CAE}(\mathbf{z}). \tag{2}$$

The autoencoder should be forced to reconstruct the input image, therefore the mean squared error (MSE) function is used as the guiding loss function. The MSE-loss is the squared l^2-norm between each pixel of the input $\mathbf{x}$ and the reconstructed image $\tilde{\mathbf{x}}$, where $\mathbf{x}(m,n)$ and $\tilde{\mathbf{x}}(m,n)$ denote the intensity at the pixel locations (m,n) with $m \in [1,...,H]$ and $n \in [1,...,W]$ of image $\mathbf{x}$ and $\tilde{\mathbf{x}}$, respectively (Rumelhart and McClelland, 1987; Bergmann et al., 2019; Bank et al., 2020; Manakov et al., 2019):

$$\mathcal{L}_{MSE}(\mathbf{x},\tilde{\mathbf{x}}) = \frac{1}{H}\frac{1}{W}\sum_{m=1}^{H}\sum_{n=1}^{W}(\mathbf{x}(m,n)-\tilde{\mathbf{x}}(m,n))^2. \tag{3}$$

2.2 Variational Autoencoder

Similarly to the CAE, the variational autoencoder (VAE) as described in Kingma and Welling (2014), Rocca (2019) and Pereira and Silveira (2018) consists of an encoder E_{VAE}, which learns a latent representation of the input, and a decoder D_{VAE}, which generates an output based on the latent variables. The network is trained to encode and decode the input $\mathbf{x}$ in such a way that the reconstructed input $\tilde{\mathbf{x}}$ is as similar as possible to $\mathbf{x}$. In contrast to the CAE, the VAE not only compresses the input to a lower dimensional representation, but encodes it as a distribution over the latent space. More precisely, the latent representation $\mathbf{z}$ of an input is now constrained to be a random variable distributed according to a prior distribution $p_\theta(\mathbf{z})$, which is typically a Gaussian distribution $\mathcal{N}(\mu,\sigma)$. For a continuous latent space, the true posterior $p_\theta(\mathbf{z}|\mathbf{x})$ is intractable. A deterministic approximation $q_\Phi(\mathbf{z}|\mathbf{x})$ can be found by applying the variational inference technique, a technique to approximate complex distributions. Loosely speaking, the idea is to set a parametrised family of distributions and to look for the best approximation of the target distribution among this family, i.e. the element of the family that gives the least approximation error. To learn the autoencoder's parameters, we optimise the following:

$$\mathcal{L}(\theta,\phi,\mathbf{x}) = \mathbb{E}_{q_\Phi(\mathbf{z}|\mathbf{x})}[p_\theta(\mathbf{x}|\mathbf{z})] - \mathcal{D}_{KL}(q_\Phi(\mathbf{z}|\mathbf{x})||p_\theta(\mathbf{x})). \quad (4)$$

The first term of this loss function is the reconstruction loss, which measures how well the input was reconstructed. The second term is the Kullback–Leibler divergence. It evaluates how much information is lost if p_θ is approximated by $q_\Phi(\mathbf{z}|\mathbf{x})$. It makes sure that the learned distribution stays close to the prior distribution. The reconstruction loss can be simplified to the MSE loss (given previously in equation 3) if $q_\Phi(\mathbf{z}|\mathbf{x})$ is following a Gaussian distribution. Kingma and Welling (2014) show how the Kullback–Leibler divergence can be simplified when both prior and posterior approximations are assumed to be distributed according to a Gaussian distribution. Variance σ and mean μ will be learned according to the following equation, where J is the number of elements in vectors σ and μ:

$$\begin{aligned} &-\mathcal{D}_{KL}(q_\Phi(\mathbf{z}|\mathbf{x})||p_\theta) = \\ &\frac{1}{2}\sum_{j=1}^{J}(1+\log((\sigma_j)^2)-(\mu_j)^2-(\sigma_j)^2). \end{aligned} \quad (5)$$

2.2.1 Re-parametrization Trick

As the decoder samples randomly from $\mathbf{z} \sim q_\Phi(\mathbf{z}|\mathbf{x})$, we need to backpropagate through this random sampling operation in order to train the network. However, backpropagation can not flow through a random node. The re-parametrization trick was proposed by Kingma and Welling (2014) and is commonly used (Rocca, 2019; Pereira and Silveira, 2018) to bypass this problem by describing the random variable $\mathbf{z}$ as a differentiable transformation of another random variable ε.

The distribution of ε is independent of $\mathbf{z}$, and Φ and $\mathbf{z}$ are given. If one assumes $q_\Phi(\mathbf{z}|\mathbf{x}) = \mathcal{N}(\mathbf{z};\mu,\mathrm{diag}(\sigma^2))$, then, after parametrization with $\varepsilon \sim \mathcal{N}(0,\mathbf{I})$, the latent representation can be computed as in eq. 6. μ and $\log(\sigma)$ are outputs of the encoder network.

$$\mathbf{z} = \mu + \sigma \odot \varepsilon \quad (6)$$

2.3 Adversarial Autoencoder

Similarly to the VAE, the adversarial autoencoder (AAE) proposed by Makhzani et al. (2016) imposes a prior distribution on the latent vector $\mathbf{z}$. Both probabilistic autoencoders match the aggregated posterior of the hidden code vector with a prior distribution. While the VAE does this by applying the Kullback-Leibler divergence, the AAE uses Generative Adversarial Networks (GAN) (Goodfellow et al., 2014). The AAE is a composite of a "standard" convolutional autoencoder and an adversarial network which regularizes the encoded vector. The autoencoder attempts to minimize the reconstruction error. Additionally, the encoder E_{AAE} of the autoencoder is the generator of the adversarial network and ensures that the discriminative adversarial network C_{AAE} can be "fooled into thinking" that the hidden code comes from the true prior distribution.
Both the autoencoder and the adversarial network are trained jointly in two phases - a *reconstruction* phase and a *regularization* phase.
During the *reconstruction* phase, E_{AAE} and D_{AAE} are optimised in the exact same way as E_{CAE} and D_{CAE} - the parameters are updated to minimize the reconstruction error as given in Eq. 3.

In the *regularization* phase, the adversarial network is trained. The discriminative model C_{AAE} of this network does not directly discriminate between "real" and "fake" data but acts as a critic. It estimates the distance between training data distribution and the distribution generated by E_{AAE} by computing the Wasserstein distance as described in Arjovsky et al. (2017). To enforce the Lipschitz constraint, the weights are clipped to a fixed box after each gradient update. The discriminative network is trained to distinguish between "true samples" $\mathbf{z}$, generated based on the prior, and the hidden representation of input data $\tilde{\mathbf{z}}$ computed by E_{AAE}. Then the adversarial network updates its generator E_{AAE} to confuse the discriminator C_{AAE} (Makhzani et al., 2016; Arjovsky et al., 2017).

3 COMPARISON OF DIFFERENT AUTOENCODER TYPES FOR ANOMALY DETECTION

In order to compare the CAE with the VAE as well as the AAE, their architectures are chosen to be in an identical manner. Detailed information about the networks' architectures are given in the appendix. The encoders of CAE, VAE and AAE are implemented in an identical manner. Their computed latent representations are mapped back to the image domain by identical decoders for CAE, VAE and AAE (Tab. 2). The bottleneck architecture of the VAE is implemented based on the exact same architecture as for the CAE and AAE, except that there are not just one but two innermost linear layers for σ and μ, respectively (Tab. 3). These values are then reparametrized for the VAE. The architecture of the C_{AAE} is given in Tab. 4. The size of the convolutional kernels was chosen to be 3×3.

All networks were trained on the same images for the same number of epochs, with the same architecture parameters and with the same learning rate and minibatch size. The Adam algorithm as proposed in Kingma and Ba (2014) was used to optimize the parameters of the models.

3.1 Experiments on Synthetic Datasets

Both synthetic datasets include four non-anomalous images with a ground structure considered as normal and four images where the ground structure was changed in order to create anomalies (Fig. 2). The anomalous regions of the first dataset, which we will refer to as the *chess*-dataset, are composed of repetitive sequences of black and white squares of the same size. The anomalous regions were generated by applying elastic deformations as described by Simard et al. (2003): displacement vector fields were computed by randomly selecting values from a uniform distribution and a subsequent convolution with a Gaussian kernel.

The non-anomalous images of the second dataset will be referred to as *noise*-dataset. It consists of four images with intensity values drawn from a Gaussian distribution. The anomalous regions were induced by plotting a noisy linear function on top of it (Fig. 2).

All three autoencoder types were trained on the non-anomalous images. The trained model was then applied to the anomalous examples, $\mathbf{R}(\mathbf{x}, \tilde{\mathbf{x}})$ was used to locate the anomalies. In order to compute a binary detection mask $\mathbf{R}_t(\mathbf{x}, \tilde{\mathbf{x}})$, $\mathbf{R}(\mathbf{x}, \tilde{\mathbf{x}})$ was thresholded by a constant t, which was chosen s.t. the *IoU* (see paragraph 3.1.1) was maximized.

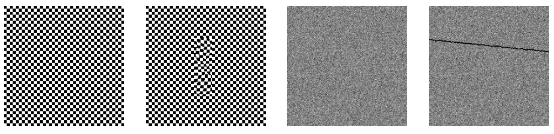
(a) (b) (c) (d)

Figure 2: Examples of non-anomalous images (Fig. 2a and Fig. 2c) and their corresponding anomalous images (Fig. 2b and Fig. 2d) of our synthetic datasets.

3.1.1 Evaluation Metrics

As the anomalies were induced by ourselves, we had an accurate two-dimensional ground truth available. We consider how accurately the residual maps capture the anomalous regions by means of accuracy $\mathcal{A}$ and intersection over union IoU. $\mathcal{A}$ is the average number of correctly classified pixels. If we denote the binary segmentation result as $\mathbf{R}_t(\mathbf{x}, \tilde{\mathbf{x}}) \in \mathbb{R}^{H \times W}$ and the corresponding ground truth as $\mathbf{y} \in \mathbb{R}^{H \times W}$, we can compute $\mathcal{A}$ as follows (Ulku and Akagunduz, 2019):

$$\mathcal{A}(\mathbf{R}_t(\mathbf{x}, \tilde{\mathbf{x}}), \mathbf{y}) = \frac{1}{k} \sum_{m,n} \delta(\mathbf{R}_t(m,n), \mathbf{y}(m,n)),$$
$$\text{with } \delta(i,j) = \begin{cases} 1 & \text{if } i = j = 1 \\ 0 & \text{else} \end{cases}, \tag{7}$$

where (m,n) denote the pixel positions with $m \in [1,H]$ and $n \in [1,W]$. The variable k represents the total amount of pixels with an intensity value equal to 1 in the ground truth image $\mathbf{y}$. The *IoU* is the "overlapping" area of $\mathbf{R}_t(\mathbf{x}, \tilde{\mathbf{x}})$ and ground truth $\mathbf{y}$ divided by the area of union between $\mathbf{R}_t(\mathbf{x}, \tilde{\mathbf{x}})$ and $\mathbf{y}$ and can be written as follows (Rezatofighi et al., 2019):

$$IoU(\mathbf{R}_t(\mathbf{x}, \tilde{\mathbf{x}}), \mathbf{y}) = \frac{|\mathbf{R}_t \cap \mathbf{y}|}{|\mathbf{R}_t \cup \mathbf{y}|}. \tag{8}$$

Both $\mathcal{A}$ and IoU scale between 0 and 1. For a perfect result, $\mathcal{A} = 1$ and $IoU = 1$.

3.2 Experiments on Industrial Datasets

Images of two different industrial materials, namely *material 1* and *material 2*, were used to investigate our three convolutional autoencoders with respect to their quality inspection capability. The autoencoders were trained on defect-free images of the materials, the trained autoencoders were then applied to images showing erroneous regions. The pixelwise reconstruction error was used to locate defects in the images.

Material 1. is an aluminium plate with a translucent riblet foil attached. A riblet foil is a functional three dimensional surface ("shark skin"), which can be attached to different materials in order to reduce drag on surfaces such as wind turbines or airplane wings. They are frequently used in bionics (Bechert and Hage, 2006) and hence a highly relevant industrial application. We acquired ten albedo images of rather defect free regions of the riblet material and four albedo images of defective riblet material. Additionally, three surface normal images of non-damaged material and two images of defective material were generated. The albedo images $\mathbf{A} \in \mathbb{R}^{1\times H\times W}$ have one intensity value per channel. The surface normal images are three-channel images, $\mathbf{N} \in \mathbb{R}^{3\times H\times W}$. The surface normal components along x- and y-direction are stored in the first and second colour channel, respectively. The z-component is stored in the third channel. Patches of size 128 $\times$ 128 pixel were sampled randomly from the images of size 5496 $\times$ 3672 pixel during training (Fig. 3).

Material 2. is a steel plate with a surface of a specific granularity texture. Steel products are employed in various manufacturing sectors (Hidalgo and Kamiński, 2011) and a detection of defective material is highly applicable. For this material, one pair of gradient and corresponding curvature image of defect-free and an image pair with gradient and curvature image of defective material were acquired with a photometric stereo set-up. The images have dimensions 2336 $\times$ 4000 pixel. We used 128 $\times$ 128 pixel patches as input images (Fig. 3).

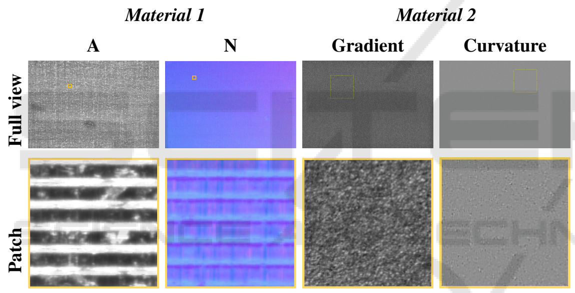

Figure 3: Examples of an albedo image **A** and a surface normal image **N** of *material 1* and a gradient and curvature image of *material 2* are shown. We sampled patches as shown in the second row for model training.

4 RESULTS

In this section, we demonstrate the quantitative and qualitative performance of our three autoencoder types as introduced in Sec. 2 on the datasets we introduced in Sec. 3.

4.1 Synthetic Datasets

First, we present the quantitative and qualitative autoencoder performance on our synthetic ground truth datasets. We evaluate how accurate our models detects anomalous regions and how long the training takes.

4.1.1 Qualitative Results

All of our three autoencoder types detected the anomalous regions for both datasets well, but especially for our *noise* dataset, there were several non-anomalous pixels insufficiently well reconstructed, see Fig. 4.

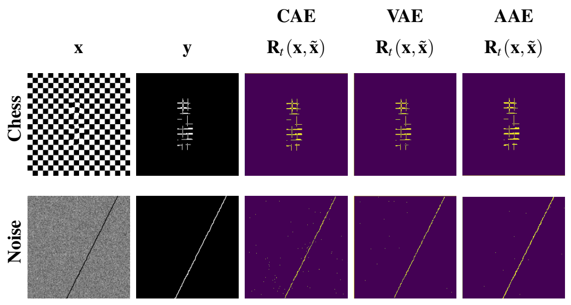
CAE
VAE
AAE
x
y
$\mathbf{R}_t(\mathbf{x},\tilde{\mathbf{x}})$
$\mathbf{R}_t(\mathbf{x},\tilde{\mathbf{x}})$
$\mathbf{R}_t(\mathbf{x},\tilde{\mathbf{x}})$
Chess
Noise
Figure 4: Illustration of $\mathbf{R}_t(\mathbf{x},\tilde{\mathbf{x}})$ of all our autoencoder types on both synthetic datasets. The anomalous regions of images are highlighted in their corresponding ground truth images. $\mathbf{R}_t(\mathbf{x},\tilde{\mathbf{x}})$ of the different networks capture the anomalous regions.

4.1.2 Quantitative Results

By computing $\mathcal{A}(\mathbf{R}_t,\mathbf{y})$ and $IoU(\mathbf{R}_t,\mathbf{y})$, we can evaluate the anomaly detection performance in a quantitative manner. Both scale between 0 and 1, a higher value represents superior results.
The values given in Tab. 1 show that, while all models perform quite well, the AAE performs best for both datasets. The performance differences are only marginal for the *chess* dataset. For the more complex *noise* dataset, both CAE and VAE are outperformed significantly by the AAE. The anomalous region in the *chess* dataset is detected more accurately than the anomalous region in the *noise* dataset.

We measured the training times $time_{tr}$ for all three autoencoder types and for both datasets. The last column in Tab. 1 shows that the training of the CAE is faster than training the VAE and the AAE.
This is of course reasonable, the training procedure of the CAE is the simplest and the least computation steps are necessary. The VAE needs more computations due to the re-parametrization of the latent variables. Training the AAE is the most expensive procedure since we do not only train an encoder and a decoder, but also the adversarial network component.

4.2 Industrial Datasets

In this subsection, we evaluate our three autoencoder types on our self-acquired industrial datasets. For this

Table 1: Evaluation of the anomaly detection on our synthetic datasets using $\mathcal{A}$ and IoU. The last column shows the time needed for training the models (in seconds).

	Metric / Type	$\mathcal{A}(\mathbf{R}_t(\mathbf{x},\tilde{\mathbf{x}}),\mathbf{y})$	$IoU(\mathbf{R}_t(\mathbf{x},\tilde{\mathbf{x}}),\mathbf{y})$	$Time_{tr}$
chess	CAE	0.9487	0.7975	**212**
	VAE	0.9492	0.7995	213
	AAE	**0.9499**	**0.7998**	1223
noise	CAE	0.9093	0.7594	**216**
	VAE	0.8797	0.7698	220
	AAE	**0.9218**	**0.7743**	1227

purpose, we generated image samples of two different materials, namely *material 1* and *material 2*.

Material 1. is a riblet foil mounted on a metal plate, see section 3.2 for more detailed information. Fig. 5 show that the convolutional autoencoder is able to learn that albedo images (see Sec. 3.2) consist of alternating dark and bright horizontal tracks. When the trained model is applied to images with defects, the model fails to reconstruct the defective regions. The autoencoder reconstructs these anomalous regions as if they were normal.

Unfortunately, there is no ground truth available which clearly states where defective regions are. As we wanted to get an idea of how well we are able to distinguish defective patches from non-defective patches, bounding boxes were drawn around defective regions. Fig. 6 shows histograms computed by averaging the reconstruction error of defective and non-defective patches. The histogram corresponding to the albedo images suggests that significantly higher reconstruction errors are computed for anomalous patches and that our model could potentially distinguish between defective and non-defective image regions rather well. A distinction between normal and defective patches is more difficult for surface normal images. Although some anomalous patches were reconstructed significantly worse than most non-anomalous patches, there are several non-anomalous patches which were reconstructed nearly as poorly as the "most anomalous" (highest reconstruction error) patches.

Fig. 7 shows qualitative results of an albedo image with defective regions. Both vertical defects lead to high reconstruction errors. There are several notably darker areas in the albedo image, one is highlighted in Fig. 7. These regions were not considered as anomalous and similar structures were present in the images the autoencoder was trained on. One can observe, that although the reconstruction loss is slightly higher at these image regions, because the regions were not present on all images, the reconstruction loss is significantly higher at the pixel positions of the vertical defects the model has never seen during training.

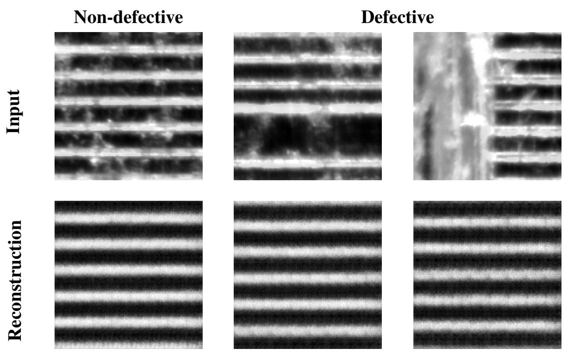

Figure 5: Illustration of normal and anomalous patches of an albedo image and their reconstructions computed by our trained CAE. The model reconstructs non-anomalous and anomalous patches in the exact same way.

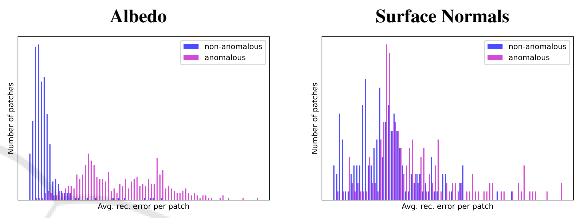

Figure 6: The histograms show the averaged reconstruction loss per patch for patches sampled of non-anomalous and anomalous regions of albedo and surface normal image.

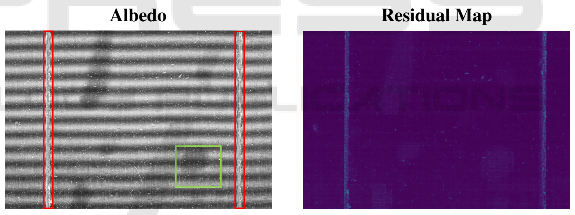

Figure 7: Illustration of an albedo image with a defective region and the corresponding residual map. The defective regions are highlighted with red boxes in the input image. The region highlighted with a green box was not categorized as anomalous, similar structures were present during training.

Material 2. is a steel plate with a specific granularity texture we describe in more detail in paragraph 3.2. We utilize it to investigate the training process on one of our autoencoder types. For this demonstration we chose the CAE. Both other types computed comparable outcomes. Fig. 8 shows how the output of our CAE model develops during training. One can see that the model is not able to capture any regularity in the images and starts to just put the averaged intensity value on all pixel positions for both gradient and curvature image. As the model did not learn to reconstruct the normal structure properly, it also fails to detect the anomalous image regions since both non-defective and defective regions are reconstructed poorly, see Fig. 9.

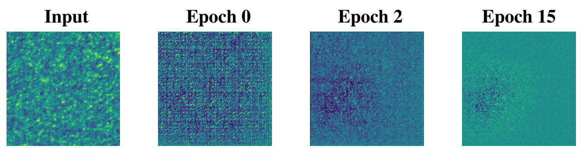

Figure 8: Illustration of the reconstruction of an input patch of the gradient image computed by the CAE at different epochs. The training of the CAE on the curvature image showed the same “averaging” behaviour.

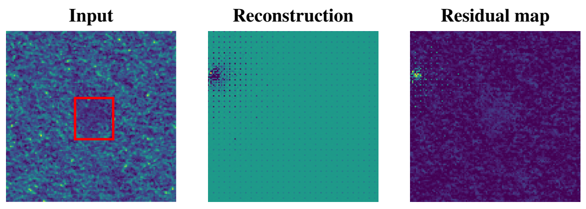

Figure 9: Illustration of a gradient input patch with a defective region marked in red, its reconstructions and residual map.

5 CONCLUSIONS

In this paper we investigated the autoencoder in different anomaly detection scenarios. To this end, we compared convolutional versions of the CAE, the VAE and the AAE.
On our synthetic and industrial datasets, we demonstrated that the autoencoders can be used effectively to locate defects by computing the two-dimensional residual map, but only if there is enough regular geometric structure. All of our autoencoders were capable to compute an accurate detection of the anomalous image regions. For the anomaly detection in the albedo and surface normal images of the first industrial dataset *material 1*, the autoencoders achieved good results as well. However, the autoencoder models did not compute any reasonable reconstructions for *material 2*. The autoencoders can not identify a regular pattern in the data and the least costly result they can reconstruct is an image with intensity values equal to the averaged value of the input image (see Fig. 8). If there is no accurate reconstruction of the normal image structure computed, the residual map does not include any reasonable anomaly detection information, see Fig. 9. Interestingly, the model seems to find a pattern in the synthetically generated noise pattern. We argue that the reason for this lies in its partial regularity in structure due to its computational generation process. The CAE is the simplest model demanding the simplest training procedure. This is reflected in the measured training times, which are the shortest compared to VAE and AAE. The training of the VAE model takes longer due to the re-parametrisation step. Training the AAE takes the longest, because the adversarial component needs to be trained additionally. For the synthetic datasets, the AAE detects the anomalous regions best for both *noise* and *chess* dataset. However, one could argue that the increase in performance is too subtle to justify the use of a more complex model.
Although we find the autoencoders versatility particularly convincing, we could also get an insight on applications where it is not suitable as a tool for anomaly detection. Namely, if the data lacks any kind of regularity, the model can not identify a meaningful compression of the data. Additionally we want to mention that although the autoencoder is trained in an unsupervised manner, compiling a training set with images of purely non-defective material can be demanding. Even for experts it is challenging to tell if certain structures should be considered as normal for industrial datasets.

Remarks. In order to examine and compare the defect detection capabilities of autoencoders further, we strongly depend on the annotation of our industrial datasets. Such industrial annotation comparison will be a part of the scope of our future work. Also we are aware that model architecture parameters, such as the size of the latent layer, may have a significant impact on results. However, the same parameters were used for each “session of experiments” and their comparison can still be considered to be fair.

ACKNOWLEDGEMENTS

This work was partly funded by the Austrian Research Promotion Agency (FFG) within the project RiSPECT (874163).

REFERENCES

Arjovsky, M., Chintala, S., and Bottou, L. (2017). Wasserstein generative adversarial networks. *Proceedings of the 34th International Conference on Machine Learning*, 70:214–223.

Bank, D., Koenigstein, N., and Giryes, R. (2020). Autoencoders. *CoRR*, abs/2003.05991.

Bechert, D. W. and Hage, W. (2006). Drag reduction with riblets in nature and engineering. *Flow Phenomena in Nature Volume 2: Inspiration, Learning and Application*.

Bergmann, P., Löwe, S., Fauser, M., Sattlegger, D., and Steger, C. (2019). Improving unsupervised defect segmentation by applying structural similarity to autoencoders. *Proceedings of the 14th International Joint Conference on Computer Vision, Imaging and Computer Graphics Theory and Applications*.

Essid, O., Samir, C., and Hamid, L. (2018). Automatic detection and classification of manufacturing defects in metal boxes. *PLOS ONE*.

Gondara, L. (2016). Medical image denoising using convolutional denoising autoencoders. *2016 IEEE 16th International Conference on Data Mining Workshops (ICDMW)*, pages 241–246.

Goodfellow, I., Pouget-Abadie, J., Mirza, M., Xu, B., Warde-Farley, D., Ozair, S., Courville, A., and Bengio, Y. (2014). Generative adversarial networks. *Advances in Neural Information Processing Systems*, 3.

Hidalgo, I. and Kamiński, J. (2011). The iron and steel industry: A global market perspective. *Mineral Resources Management*.

Kholief, E., Darwish, S., and Fors, M. (2017). Detection of steel surface defect based on machine learning using deep auto-encoder network. *7th International Conference on Industrial Engineering and Operations Management(IEOM)*.

Kingma, D. and Ba, J. (2014). Adam: A method for stochastic optimization. *International Conference on Learning Representations*.

Kingma, D. P. and Welling, M. (2014). Auto-encoding variational bayes. *CoRR*, abs/1312.6114.

Makhzani, A., Shlens, J., Jaitly, N., Goodfellow, I., and Frey, B. (2016). Adversarial autoencoders. *ArXiv*, abs/1511.05644.

Manakov, I., Rohm, M., and Tresp, V. (2019). Walking the tightrope: An investigation of the convolutional autoencoder bottleneck. *ArXiv*, abs/1911.07460.

Pang, G., Shen, C., Cao, L., and Hengel, A. V. D. (2021). Deep learning for anomaly detection. *ACM Computing Surveys*, 54(2):1–38.

Pereira, J. and Silveira, M. (2018). Unsupervised anomaly detection in energy time series data using variational recurrent autoencoders with attention. *2018 17th IEEE International Conference on Machine Learning and Applications (ICMLA)*, pages 1275–1282.

Rezatofighi, H., Tsoi, N., Gwak, J., Sadeghian, A., Reid, I., and Savarese, S. (2019). Generalized intersection over union: A metric and a loss for bounding box regression. *2019 IEEE/CVF Conference on Computer Vision and Pattern Recognition (CVPR)*, pages 658–666.

Rocca, J. (2019). Understanding variational autoencoders (vaes) - building, step by step, the reasoning that leads to vaes.

Rumelhart, D. E. and McClelland, J. L. (1987). Learning internal representations by error propagation. *Parallel Distributed Processing: Explorations in the Microstructure of Cognition: Foundations*, pages 318–362.

Simard, P., Steinkraus, D., and Platt, J. (2003). Best practices for convolutional neural networks applied to visual document analysis. *Seventh International Conference on Document Analysis and Recognition, 2003. Proceedings.*, pages 958–963.

Ulku, I. and Akagunduz, E. (2019). A survey on deep learning-based architectures for semantic segmentation on 2d images. *arXiv: Computer Vision and Pattern Recognition*.

Yang, J., Li, S., Wang, Z., Dong, H., Wang, J., and Tang, S. (2020). Using deep learning to detect defects in manufacturing: A comprehensive survey and current challenges. *Materials*, 13:5755.

APPENDIX

Table 2: Encoder and decoder architecture used for our synthetic datasets ($d = 16$) and the industrial datasets. $n_c = 3$ for the surface normal images of *material 1* and $n_c = 1$ for the albedo images of *material 1* and gradient and curvature images of *material 2*.

		Layer	Resolution	Channels	Input	Activ. func.
Synthetic dataset	Encoder	conv1	$W \times H / W \times H$	1/16	Image	Leaky ReLU
		conv2	$\frac{W}{2} \times \frac{H}{2} / \frac{W}{2} \times \frac{H}{2}$	16/32	conv1	Leaky ReLU
		conv3	$\frac{W}{4} \times \frac{H}{4} / \frac{W}{4} \times \frac{H}{4}$	32/64	conv2	Leaky ReLU
		conv4	$\frac{W}{4} \times \frac{H}{4} / \frac{W}{d} \times \frac{H}{d}$	64/64	conv3	Leaky ReLU
		conv5	$\frac{W}{d} \times \frac{H}{d} / \frac{W}{16} \times \frac{H}{d}$	64/16	conv4	Leaky ReLU
			Bottleneck			
	Decoder	deconv1	$\frac{W}{d} \times \frac{H}{d} / \frac{W}{d} \times \frac{H}{d}$	16/64	lin4	Leaky ReLU
		deconv2	$\frac{W}{d} \times \frac{H}{d} / \frac{W}{4} \times \frac{H}{4}$	64/64	deconv1	Leaky ReLU
		deconv3	$\frac{W}{4} \times \frac{H}{4} / \frac{W}{2} \times \frac{H}{2}$	64/32	deconv2	Leaky ReLU
		deconv4	$\frac{W}{2} \times \frac{H}{2} / W \times H$	32/16	deconv3	Leaky ReLU
		deconv5	$W \times H / W \times H$	16/1	deconv4	Sigmoid
Industrial dataset	Encoder	conv1	$W \times H / W \times H$	n_c/16	Image	Leaky ReLU
		conv2	$W \times H / W \times H / \frac{W}{2} \times \frac{H}{2}$	16/32	conv1	Leaky ReLU
		conv3	$\frac{W}{2} \times \frac{H}{2} / \frac{W}{4} \times \frac{H}{4}$	32/64	conv2	Leaky ReLU
		conv4	$\frac{W}{4} \times \frac{H}{4} / \frac{W}{8} \times \frac{H}{8}$	64/64	conv3	Leaky ReLU
		conv5	$\frac{W}{8} \times \frac{H}{8} / \frac{W}{16} \times \frac{H}{16}$	64/64	conv4	Leaky ReLU
		conv6	$\frac{W}{16} \times \frac{H}{16} / \frac{W}{16} \times \frac{H}{16}$	64/16	conv5	Leaky ReLU
			Bottleneck			
	Decoder	deconv1	$\frac{W}{16} \times \frac{H}{16} / \frac{W}{16} \times \frac{H}{16}$	16/64	lin4	Leaky ReLU
		deconv2	$\frac{W}{16} \times \frac{H}{16} / \frac{W}{8} \times \frac{H}{8}$	64/64	deconv1	Leaky ReLU
		deconv3	$\frac{W}{8} \times \frac{H}{8} / \frac{W}{4} \times \frac{H}{4}$	64/64	deconv2	Leaky ReLU
		deconv4	$\frac{W}{4} \times \frac{H}{4} / \frac{W}{2} \times \frac{H}{2}$	64/32	deconv3	Leaky ReLU
		deconv5	$\frac{W}{2} \times \frac{H}{2} / W \times H$	32/16	deconv4	Leaky ReLU
		deconv6	$W \times H / W \times H$	16/n_c	deconv5	Sigmoid

Table 3: *Bottleneck* architectures used for our synthetic datasets (conv$_b$ = conv5, $r = 1024$, $n_z = 100$) and the industrial datasets (conv$_b$ = conv6, $r = 1024$, $n_z = 100$).

AE type	Layer	Resolution	Input	Activ. func.
CAE/AAE	lin1	$1 \times \frac{W}{16} * \frac{H}{16} * 16 / 1 \times 1024$	conv$_b$ (flattened)	Leaky ReLU
	lin2	$1 \times r / 1 \times n_z$	lin1	-
	lin3	$1 \times n_z / 1 \times r$	lin2	Leaky ReLU
	lin4	$1 \times r / 1 \times \frac{W}{16} * \frac{H}{16} * 16$	lin3	Leaky ReLU
VAE	lin1	$1 \times \frac{W}{16} * \frac{H}{16} * 16 / 1 \times 1024$	conv$_b$ (flattened)	Leaky ReLU
	lin21	$1 \times r / 1 \times n_z$	lin1	-
	lin22	$1 \times r / 1 \times n_z$	lin1	-
	lin3	$1 \times n_z / 1 \times r$	lin21, lin22 (reparam.)	Leaky ReLU
	lin4	$1 \times r / 1 \times \frac{W}{16} * \frac{H}{16} * 16$	lin3	Leaky ReLU

Table 4: Architecture of the C_{AAE} used for all our datasets.

Layer	Resolution	Channels	Input	Activ. func.
lind1	$1 \times n_z / 1 \times 10$	-	lin2	Leaky ReLU
lind2	$1 \times 10 / 1 \times 1$	-	lind1	Leaky ReLU